World Academy of Science, Engineering and Technology
International Journal of Energy and Environmental Engineering
Vol:18, No:8, 2024

Dynamic Simulation of a Hybrid Wind Farm with Wind Turbines and Distributed Compressed Air Energy Storage System

Eronini Umez-Eronini

Abstract**—**Compressed air energy storage (CAES) coupled with wind farms have gained attention as a means to address the intermittency and variability of wind power. However, most existing studies and implementations focus on bulk or centralized CAES plants. This study presents a dynamic model of a hybrid wind farm with distributed CAES, using air storage tanks and compressor and expander trains at each wind turbine station. It introduces the concept of a distributed CAES with linked air cooling and heating, and presents an approach to scheduling and regulating the production of compressed air and power in such a system. Mathematical models of the dynamic components of this hybrid wind farm system, including a simple transient wake field model, were developed and simulated using MATLAB, with real wind data and Transmission System Operator (TSO) absolute power reference signals as inputs. The simulation results demonstrate that the proposed ad hoc supervisory controller is able to track the minute-scale power demand signal within an error band size comparable to the electrical power rating of a single expander. This suggests that combining the global distributed CAES control with power regulation for individual wind turbines could further improve the system's performance. The round trip electrical storage efficiency computed for the distributed CAES was also in the range of reported round trip storage electrical efficiencies for improved bulk CAES. These findings contribute to the enhancement of efficiency of wind farms without access to large-scale storage or underground caverns.

Keywords**—**Distributed CAES, compressed air, energy storage, hybrid wind farm, wind turbines, dynamic simulation.

NOMENCLATURE

A	Area (m^2)
p	Pressure (Pa)
B	Torsional damping constant (kg m^2 rad^{-1} s^{-1})
r	Radius (m)
F	Friction factor (kg m^2/s)
t	Time (s)
FAR	Fuel-air ratio (-)
u	Specific internal energy (J/kg)
I	Moment of inertia (kg m^2)
v	Velocity (m/s)
K	Torsional stiffness constant (kg m^2)
w	Specific work (J/kg)
LHV	Lower heating value (J/kg)
x	Longitudinal (parallel to prevailing wind direction) coordinate of wind turbine
M	Mass (kg)
N	Speed ratio (-)
y	Transverse coordinate of wind turbine
P	Power (W)
z	Elevation (m)
PR	Pressure ratio (-)
Ω	Angular velocity (deg/s)
$\dot{Q}$	Heat transfer rate (W)
Γ	Time constant; time step (s)
R	Specific gas constant for air (287.052874 J kg^{-1} K^{-1})
β	Collective pitch angle (deg)
γ	Torsional angle (rad)
T	Temperature (K)
λ	Tip speed ratio (-)
V	Volume (m^3)
η	Efficiency (-)
c_p	Specific heat (J kg^{-1} K^{-1})
φ	Coefficient in compressor control torque–desired power relation
e	Specific energy (J/kg)
f	Frequency (Hz)
ρ	Density (kg m^{-3})
g	Acceleration due to gravity (m s^{-2})
ω	Angular speed; circular frequency (rad/s)
h	Specific enthalpy (J/kg)
k	Polytropic index; discrete-time index (-)
τ	Torque (N m)
m	Mass flowrate (kg/s)
ξ	Damping ratio (-)

I. INTRODUCTION

CONVENTIONAL CAES systems employing large scale underground formations for air storage can improve, by almost a factor of two (to about 70%), the capacity factor of onshore wind farms [1]. CAES systems have limited environmental impact and operational constraints, are long lived, and represent mature and reliable technology with high power capture advantages over most other energy storage approaches to mitigating the intermittency and availability problem of wind resources. Conventional CAES systems possess high economics of scale and reliability due to the use of proven conventional turbomachinery. They are thus economical and well suited for use in base-load wind (long-term load leveling) concepts [2], [3]. Two well known, long-operating, commercial examples are the Huntorf CAES plant in Germany and the McIntosh facility in Alabama, USA, both of which utilize solution-mined salt caverns for air storage [4]. However, favorable geologic resources for air storage are often not collocated or in close proximity with some wind farms,

Eronini Umez-Eronini is with Conrow, Inc., USA (e-mail: eroniniie@conrow.org).

especially offshore wind farms. Although offshore wind turbines operate at higher capacity factors than wind turbines on land, due to offshore higher wind speeds and other features, without energy storage, only a modest increase of capacity factor (from about 39% in 2010 to about 45% by 2030), was projected by using technology enhancements and various other production and market improvements [5].

Conventional CAES also have limited system efficiency due mostly to thermal energy losses in the air cooling system during air compression in the storage phase, and fuel energy requirement during air expansion in the power generation phase. Technological tweaks of CAES aimed at improving its cycle efficiency give rise to various categories or types of CAES. Conventional CAES, such as the McIntosh plant, which utilize intercoolers and aftercooler to reject compression heat during the charging period and combust fuel for a heat source during the discharging period, is considered of type Diabatic-CAES or D-CAES. Adiabatic-CAES or A-CAES stores the heat generated during air compression in a thermal energy storage component (TES) and utilizes the stored heat to preheat the air in the discharging period, thus reducing or completely eliminating the fuel energy requirement in this phase of the process [4], [6]-[8]. Isothermal-CAES or I-CAES seeks the highest system efficiency by replacing the conventional CAES compressor and expander with a novel component in which isothermal compression and isothermal expansion are achieved [4], [9]-[11]. A critical review of these CAES systems, as well as other thermo-mechanical energy storage systems has been conducted by Olympios et al. [12].

Most proposed novel CAES technology with potentially higher thermal system efficiencies than conventional CAES, include components that must undergo long and extensive development before these elements approach the functional and reliability levels of conventional CAES components. A distributed CAES system comprised of a multiplicity of air storage tanks, compressor and expander trains at several, if not all, wind turbine stations in a farm, retains all the capacity improvement benefits of coupling CAES with a wind farm, while utilizing available and proven components of conventional CAES. The much reduced size storage tanks at the wind turbine stations may operate at much higher pressures than is feasible with geologic formations or large consolidated storage means thus mitigating the loss of economy of scale in the distributed system. Umez-Eronini [13] describes such a hybrid wind farm system that utilizes distributed D-CAES with a thermal energy interchange network that links all the CAES stations with controlled cooling and heating circuits to boost system efficiency. It is noted that the term, distributed CAES, may also be applied to two other CAES ideas reported in the literature, which are however distinct from the present concept: (1) the hybrid wind turbine system, whereby the wind turbine shaft is connected with an air expander/compressor component of a CAES by a continuously variable transmission [14], [15] could represent a distributed CAES, with wind power dependent energy storage unit and novel, relative to conventional CAES, power train; and (2) the distributed compression concept where the D-CAES compressor is located near a (remote) heat load, with a pipe line connecting it to the air storage, in order to utilize the compression heat and thus enhance system efficiency [12], [16], [17].

II. Model Development

The Hybrid Wind Farm explored here is composed of a number of hybrid wind turbine – CAES stations linked by air cooling and heating networks. Assuming that the hybrid stations are identical, it is necessary to develop a mathematical model of only one such station. Moreover, the hybrid station model may be obtained by integrating the individual models of the station components. The component models developed in this initial study vary in detail according to their perceived impact on the overall system performance and availability of characteristic design data.

Fig. 1 is a schematic of the typical hybrid wind farm CAES-wind turbine station with the topology of the elements. The component models and simulation approaches for the hybrid wind farm with wind turbines and distributed CAES are presented, with reference to Fig. 1, under six subsystems in the following subsections: (A) Air Compression System, (B) Air Storage System, (C) Air Expansion System, (D) Heat Network, (E) Wind Turbine System, and (F) Hybrid Wind Farm System. In the present development, the same motor/generator that drives the compressors also drives/is driven by the expanders through clutch means. This represents a less flexible configuration considering the control of the system energy storage and power production, but a lower cost option with respect to component count. The respective clutch dynamics are however not modeled here. Rather, on compressor or expander start up, the motor/generator is assumed to instantaneously attain synchronous speed with the turbomachine and subsequently drive the compressor or drive the expander or be driven by the expander according to the control inputs. The design of the system configuration of Fig. 1 is represented by the parameter values summarized in Table I.

A. Air Compression System

The compressor is driven by the motor (motor/generator via a clutch) with power P_C assumed obtained from the Farm Power Circuit (FPC). The air is assumed to be compressed in only two stages; from p_1 (equal to the ambient pressure p_a), to p_2 in the Low-pressure Compressor (LpC) and from p_3 ($p_3 = p_2$, is assumed) to p_4 in the High-pressure Compressor (HpC). The air entering the LpC at temperature T_1 (equal to the ambient temperature T_a), and leaving at temperature T_2, is cooled to temperature T_3 in the Intercooler (ICR) before entering the HpC. The air leaving the HpC at temperature T_4 is cooled to temperature T_5 in the Aftercooler (ACR). The design required $T_3 = T_5 = T_{inS}$, with T_{inS} only marginally higher than the Compressed Air Storage operating temperature T_{CAS} which is in turn very close to or equal to the ambient temperature T_a (see Table I).

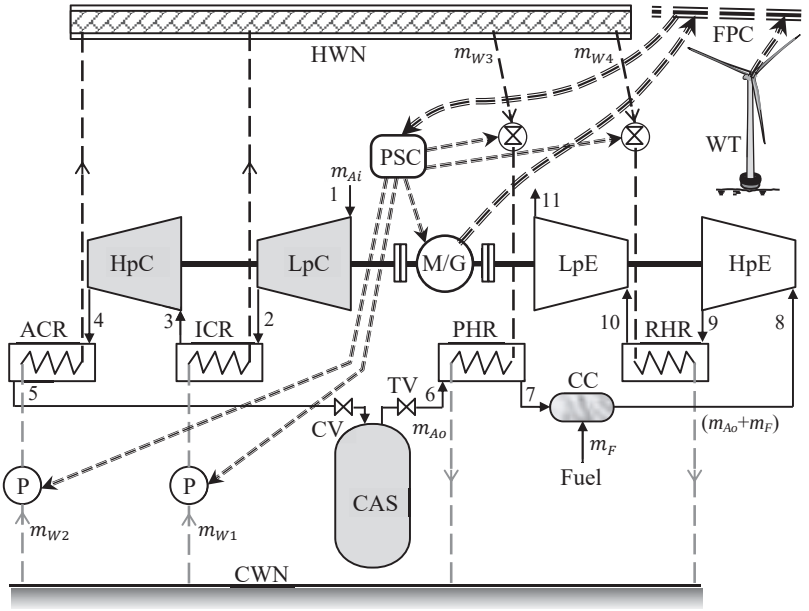

ACR	Aftercooler
CAS	Compressed Air Storage
CC	Combustion Chamber
CH	Clutch
CV	Check Valve
CWN	Cold Water Network
FPC	Farm Power Circuit
HpC	High pressure Compressor
HpE	High pressure Expander
HWN	Hot Water Network
ICR	Intercooler
LpC	Low pressure Compressor
LpE	Low pressure Expander
M/G	Motor/Generator
P	Pump
PHR	Preheater
PSC	Power Supply/Controller
RHR	Reheater
TV	Throttle Valve
WT	Wind Turbine

Fig. 1 Hybrid wind farm CAES-wind turbine station elements

TABLE I
MAIN PARAMETERS OF THE D-CAES SYSTEM

Quantity	Symbol	Value
Air storage tank design nominal inlet air temperature	T_{inS}	303.00 K
Ambient pressure	p_a	101325 Pa
Ambient temperature	T_a	298.15 K
Compressed air storage operating temperature	T_{CAS}	298.15 K
Compressor design nominal air mass flowrate	m_{CD}	6.0 kg/s
Compressor design nominal pressure ratio	PR_{CD}	9.6
Compressor motor torque acceleration power at nominal speed	$P_{TC,acc}$	4.212 MW
Equivalent CAES generator efficiency	η_G	0.944
Equivalent CAES motor efficiency	η_M	0.944
Equivalent generator-expander friction factor	F_E	0.07 kg m^2 s^{-1}
Equivalent generator-expander moment of inertia	I_E	97 kg m^2
Equivalent motor-compressor friction factor	F_C	0.124 kg m^2 s^{-1}
Equivalent motor-compressor moment of inertia	I_C	122 kg m^2
Expander design nominal air mass flowrate	m_{ED}	10.8 kg/s
Expander design nominal expansion ratio	PR_{ED}	7.2
Expander generator torque control power at nominal speed	P_{TEG}	4.296 MW
Expander motor torque control power at nominal speed	P_{TEM}	3.236 MW
High pressure expander design inlet pressure	$p_{HpE\text{-}i}$	52 atm*
High pressure expander design inlet temperature	$T_{HpE\text{-}i}$	603.15 K
Hot water network design temperature	T_{HWN}	498.15 K
Internal volume of compressed air storage tank	V_{CAS}	2001 m^3
Low pressure expander design inlet temperature	$T_{LpE\text{-}i}$	491 K
Maximum compressor motor torque control power at nominal speed	$P_{TC,max}$	4.4987 MW
Minimum compressor motor torque control power at nominal speed	$P_{TC,min}$	3.5809 MW
Nominal compressor and expander design speed	ω_{nom}	1655.41 rad/s
Preheater design exit temperature	$T_{PHR\text{-}o}$	491 K

*1 atm ≡ 101325 Pa

Mechanics: The acceleration of the compressor is given by:

$$\frac{d\omega_C}{dt} = \frac{\eta_M P_C - m_{Ai}\Delta h_C - F_C\omega_C{}^2}{I_C\omega_C} \quad (1)$$

where ω_C is the angular speed of the compressor, η_M is the equivalent motor efficiency, m_{Ai} is the compressor air mass flowrate, Δh_C is the total enthalpy change due to the air compression, F_C is the equivalent motor-compressor friction factor, and I_C is the equivalent motor-compressor moment of inertia. For a compressor allowed to charge the compressed air storage (CAS) by the control system, the air mass flowrate m_{Ai} is given by the normalized mass flowrate $m_{NC} = m_{Ai}/m_{CD}$ determined from the compressor performance map, given the current compressor speed (that is, the normalized speed N = ω_C/ω_{nom}) and the compressor design operating line. The design values of m_{CD} and ω_{nom} are in Table I.

Thermodynamics: Assuming the air is an ideal gas with specific heat that only slowly varies with temperature, the air temperatures at the outlet of the Low pressure and High pressure compressors are given by (2) and (3):

$$T_2 = T_1 + T_1\left[\left(\frac{p_2}{p_1}\right)^{\frac{k_{LC}-1}{k_{LC}}} - 1\right]\frac{1}{\eta_{isen-C}} \quad (2)$$

$$T_4 = T_3 + T_3\left[\left(\frac{p_4}{p_3}\right)^{\frac{k_{HC}-1}{k_{HC}}} - 1\right]\frac{1}{\eta_{isen-C}} \quad (3)$$

where k_{LC} and k_{HC} are polytropic indices determined from look up tables of model air properties at the respective mean temperatures ½(T_1+T_2) and ½(T_3+T_4). Note that while T_1 (=T_a) and T_3 (=T_{inS}) are set by the system configuration and design (see Table I), T_2 and T_4 are variables given by (2), and in the simulation, it is necessary to guess their values (typically taken as their values at the previous computational time step). $\eta_{isen\text{-}C}$ is the compressor isentropic efficiency determined from the

compressor performance map, using the normalized air mass flowrate and the compressor design operating line. The Low-pressure and High-pressure compressors are assumed to be configured to operate at the same pressure ratios, so that

$$\frac{p_2}{p_1} = \frac{p_4}{p_3} = PR_C \tag{4}$$

where PR_C is the compressor pressure ratio, also determined from the compressor map, using the known normalized air mass flowrate and the compressor design operating line. For ideal gas assumption,

$$\Delta h_C = c_{pLC}(T_2 - T_1) + c_{pHC}(T_4 - T_3) \tag{5}$$

where c_{pLC} and c_{pHC} are air specific heat values determined, as was the case for the polytropic index, from model air properties at the respective mean temperatures. The employed compressor map, shown in Fig. 2 was obtained by scaling with respect to the design nominal air mass flowrate, an available compressor map of a single-shaft gas turbine with compatible power output (5.71 MW) and speed (15,808 RPM), which was investigated in [18]. It is assumed the compressor is equipped with variable inlet guide vanes (IGV) and accessories that permit full control of the mass flowrate into the compressor and enable the compressor to closely follow a safe and feasible operating path on the compressor map. In this case, the operating path is taken as the horizontal (PR_C = constant = PR_{CD}) line, shown in Fig. 2. A compressor's characteristic map ordinarily changes for different positions of the IGV, and a single "average" map (as shown) may only be approximately applicable for a narrow range of compressor rotor speeds (in this case, the normalized speed range for which compressor air flow was only permitted in the simulations is $0.86 \le N < 1.05$; $N = \omega_C/\omega_{nom}$, and ω_{nom} = nominal speed = 1655.4 rad/s (or 15808 RPM).

Control: The compressor is controlled by fixing the rotor torque using feedback of the rotor speed,

$$\eta_M P_C = \left(\frac{P_{TC}}{\omega_{nom}}\right)\omega_{CF} \tag{6}$$

where ω_{CF} is the feedback signal of the compressor rotor speed ω_C, and (P_{TC}/ω_{nom}) is the control torque. The design and configuration of the compressor admit motor torque control power (at nominal speed) that may vary over a small range $P_{TC,\min} \le P_{TC} \le P_{TC,\max}$ (see Table I). For a fixed value of P_{TC}, the power consumed by the compressor settles to a steady-state value $P_{Css} = [(P_{TC}/\omega_{nom})/\eta_M]\omega_{Css}$ different from P_{TC}/η_M (see Fig. 3 (a) which shows the case $P_{TC} = P_{TC,\max}$, after the rotor speed reaches the threshold value, $\omega_C = \omega_{Ct} = 0.86\omega_{nom}$). By conducting the simulation represented by Fig. 3 (a) for different values of P_{TC} within the allowable range, an approximate functional relation between desired power consumption P_{Css} and the control torque (P_{TC}/ω_{nom}) may be obtained for use with the compressor control. In this case,

$$\left(\frac{P_{TC}}{\omega_{nom}}\right) = -5.3150 \times 10^{-11} {P_{Css}}^2 + 7.6451 \times 10^{-4} P_{Css} + 239.2653 \tag{7}$$

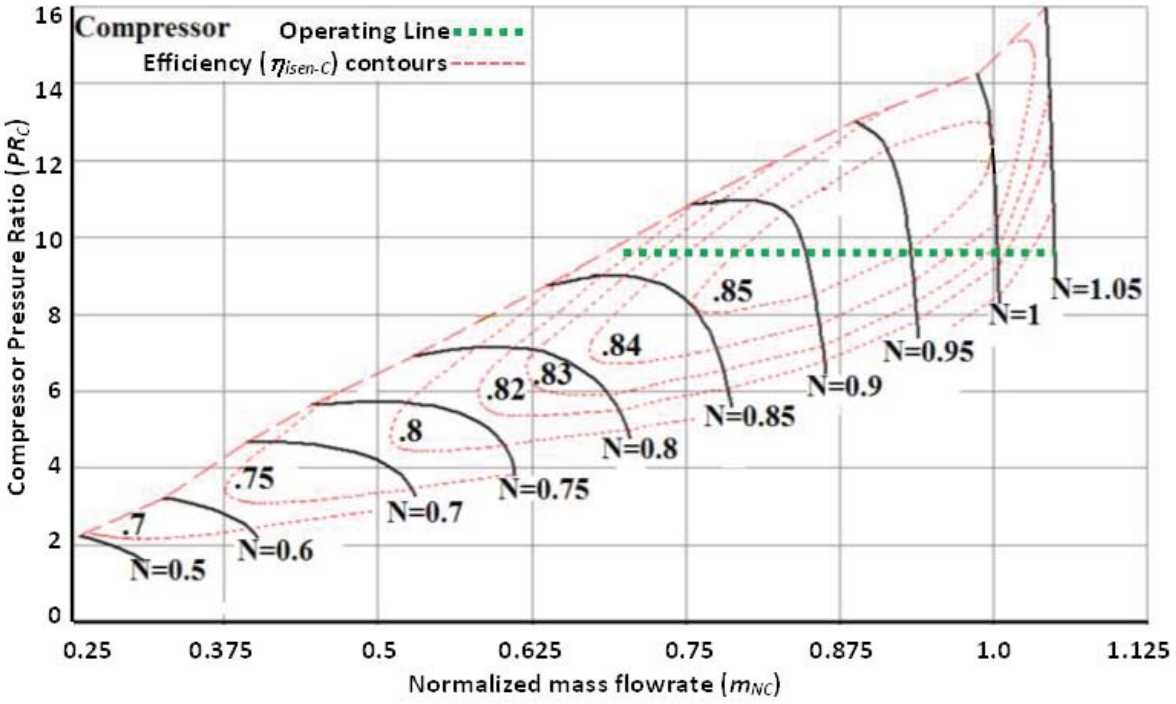

Fig. 2 Adopted compressor map and operating line

When a compressor is placed in "run" state by the hybrid farm supervisory controller, it is first accelerated from its current speed, to the threshold speed given by $N = 0.86$, without compressed air flow, using $P_{TC} = P_{TC,acc}$ (see Table I). At the

threshold speed, compressed air flow is started and is regulated according to the operating path on the compressor map as stated above, while P_{TC} is set within its limits by the supervisory (farm) controller which supplies P_{Css}. For a compressor in "not run" state, $\eta_M P_C = 0$, there is no air flow $m_{Ai} = 0$, and the compressor coasts down. A compressor whose associated air storage tank becomes full (see next segment), is commanded into "not run" state by the farm controller.

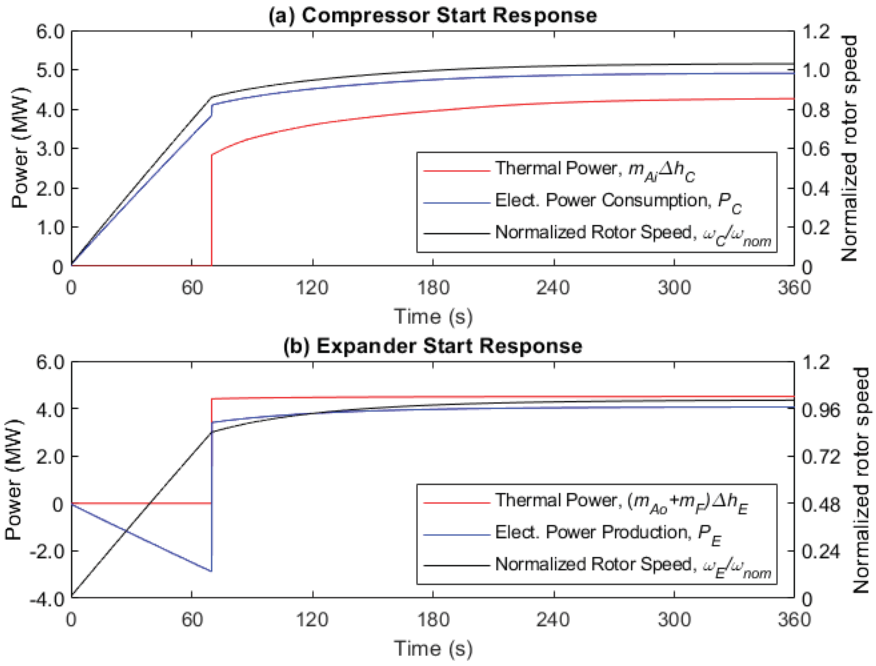

Fig. 3 Start response of CAES compressor and expander

B. Air Storage System

The air leaving the HpC enters the CAS through a check valve (CV) which permits the air to only enter the CAS and not leave through it. Consistent with [13], the compressed air is assumed to be stored in an uncompensated constant volume tank. The conservation of mass principle for the tank is,

$$\frac{dM_T}{dt} = m_{Ai} - m_{Ao} \tag{8}$$

where M_T is the mass of air in the tank and m_{Ao} is the air mass flowrate out of the tank, and into the Preheater (PHR). With the temperature of the compressed air entering the tank arranged to be at near ambient temperature, the air storage tank (insulated or otherwise) is assumed to operate at the constant temperature T_{CAS}, so that heat losses from the tank may be ignored. Also ignoring kinetic and potential energies in the tank, and flow work done by air entering or leaving the tank, the ideal gas air behavior assumption gives the pressure in the tank p_T:

$$p_T = M_T \left(R \frac{T_{CAS}}{V_{CAS}} \right) \tag{9}$$

where R is the specific gas constant for dry air and V_{CAS} is the effective volume of the air storage tank. The system configuration considered CAS operation over a nominal pressure range $52 < p_T \leq 92.16$ atm (1 atm = 101325 Pa); and a nominal charge time of the storage tank between these pressures of about 4.5 hours. These pressure extremes also define an "empty" tank or a "full" tank. With the compressor design nominal mass flowrate m_{CD} of 6.0 kg/s, the effective volume of the air storage tank was set at $V_{CAS} = 2001$ m^3 (see Table I). This storage volume can be realized, for example, in a cylindrical vessel with internal dimensions of 7 m diameter and 52 m height (excluding internal tank structural elements).

C. Air Expansion System

The generator (motor/generator via a clutch) represents a controlled load (torque τ_G) on the expander. The torque is positive when power is being generated (and sent to the FPC) but negative when the expander is merely being accelerated by the motor (using power obtained from the FPC). The load power equals $\tau_G \omega_E$, where ω_E is the expander rotor speed. The air is assumed to be expanded in two stages; from p_8 to p_9 in the High-pressure Expander (HpE) and from p_{10} to p_{11} in the Low-pressure Expander (LpE). It is assumed $p_8 = p_{HpE\text{-}i} = p_7 = p_6$; $p_9 = p_{10}$; and p_{11} is designed to be, in general, only marginally higher than p_a. With Constant Inlet Pressure operating mode adopted for the expander, the air leaving the CAS passes through a throttling control valve (TV), which maintains the exit pressure p_6 constant ($p_6 = 52$ atm) and regulates the outlet air mass flowrate m_{Ao}. Pressure loss, and hence energy loss at the throttling valve is neglected in this investigation. The air is heated from temperature T_6 (assumed equal to T_{CAS}) to temperature T_7 in the PHR. Heat is then added to the air in the combustion chamber (CC) by burning fuel (mass flowrate m_F), raising the air temperature from T_7 to the temperature T_8 at which the air with combustion products enters the HpE. The

PHR exit temperature, $T_7 = T_{PHR\text{-}o}$ and the high-pressure expander inlet temperature, $T_8 = T_{HpE\text{-}i}$ are fixed by the system configuration and design (see Table I). The air (excess air and combustion products) leaving the HpE at temperature T_9 is heated in the RHR to temperature T_{10}, which is set by the system configuration and design, $T_{10} = T_{LpE\text{-}i}$. The air entering the LpE at temperature T_{10}, is cooled by the expansion in the LpE to temperature T_{11} (which by design is generally not much higher than T_a).

Mechanics: Using the same modeling approach and air behavior assumptions employed for the compressor, the acceleration of the expander is,

$$\frac{d\omega_E}{dt} = \frac{(m_{Ao}+m_F)\Delta h_E - \tau_G\omega_E - F_E\omega_E{}^2}{I_E\omega_E} \quad (10)$$

where Δh_E is the total enthalpy change due to the air expansion (see (15)), τ_G is the generator load torque, F_E is the equivalent generator-expander friction factor, and I_E is the equivalent generator-expander moment of inertia. For an expander allowed to generate power by the control system, m_{Ao} is determined from the expander performance map, given the current expander rotor speed and the expander design operating line, and m_F is given by (12).

Thermodynamics: For a simple description of the burner or CC, the combustion in the chamber is assumed to be complete (no unburnt fuel in the products); the process is isobaric ($p_8 = p_7$) and adiabatic (all the heat goes to raise the temperature of the combustion products and no heat is transferred out of the chamber); the burner volume may be neglected; the inlet air may be considered composed of 21% Oxygen and 79% Nitrogen by volume so that each mole of Oxygen used to oxidize the fuel (hydrocarbon) is accompanied by 3.76 moles of Nitrogen, and the molecular mass of the air is thus approximately 29 kg/mole; and for the purpose of determining approximately the sensible enthalpy of combustion products as a function of temperature, the products of combustion may be considered all air. With these assumptions, and using Methane (CH_4) as the fuel, which is assumed is supplied at ambient temperature T_a to the burner, the First Law analysis of the combustion [19] yields,

$$\left(1.8125 + \tfrac{1}{FAR}\right)h_{Air}(T_8) = \tfrac{1}{FAR}h_{Air}(T_7) + [h_{Fuel}(T_a) + LHV] \quad (11)$$

where $FAR = m_F/m_{Ao}$ is the fuel-air ratio and LHV is the lower heating value of Methane. Given the fixed design values of T_7 and T_8, and employing ideal gas behavior for the combustion products, with the ambient temperature as also the property reference temperature, the requisite fuel mass flowrate may be obtained from (11) as,

$$m_F = \frac{m_{Ao}c_{p8-7}(T_{HpE-i} - T_{PHR-o})}{LHV - 1.8125c_{p8-a}(T_{HpE-i} - T_a)} \quad (12)$$

where $c_{p8\text{-}7}$ and $c_{p8\text{-}a}$ are air specific heat values determined, as before, from model air properties at the mean temperatures, ½(T_8+T_7) and ½(T_8+T_a), respectively.

The air temperatures at the outlet of the High pressure and Low-pressure expanders; and the total enthalpy change due to the air expansion, are given by (13)-(15):

$$T_9 = T_8 - \eta_{isen-E}T_8\left[1 - \left(\frac{p_8}{p_9}\right)^{\frac{k_{HE}-1}{k_{HE}}}\right] \quad (13)$$

$$T_{11} = T_{10} - \eta_{isen-E}T_{10}\left[1 - \left(\frac{p_{10}}{p_{11}}\right)^{\frac{k_{LE}-1}{k_{LE}}}\right] \quad (14)$$

$$\Delta h_E = c_{pHE}(T_8 - T_9) + c_{pLE}(T_{10} - T_{11}) \quad (15)$$

where k_{HE} and k_{LE} are polytropic indices determined from model air property look up tables at the mean temperatures ½(T_8+T_9) and ½(T_{10}+T_{11}), respectively, and c_{pHE} and c_{pLE} are air specific heat values also determined from the model air properties at the same respective mean temperatures. With $T_8 = T_{HpE\text{-}i}$ and $T_{10} = T_{LpE\text{-}i}$ specified, it is necessary to initially guess the values of T_9 and T_{11} (taken as their values at the previous computational time step) to evaluate k_{HE} and k_{LE} in (13) and (14). $\eta_{isen\text{-}E}$ is the expander isentropic efficiency determined from the expander performance map, given the normalized air mass flowrate, $m_{NE} = m_{Ao}/m_{ED}$ and the expander design operating line.

As shown in Fig. 4, the expander operating line is also set as a straight horizontal line of constant expansion ratio: $PR_E = PR_{ED}$ (see Table I), and the allowable normalized speed range for expander power production in the simulations is $0.84 \le N < 1.10$; $N = \omega_E/\omega_{nom}$. The High-pressure and Low-pressure expanders are configured to operate at the same expansion ratios, so that

$$\frac{p_8}{p_9} = \frac{p_9}{p_{10}} = PR_E = PR_{ED} \quad (16)$$

Control: The expander is controlled by fixing the generator load torque using feedback of the expander rotor speed ω_{EF},

$$P_E = \tau_G\omega_E = \begin{cases} \left(\frac{-\eta_M P_{TEM}}{\omega_{nom}}\right)\omega_{EF} & (\omega_E/\omega_{nom}) < 0.84; m_{Ao} = 0 \\ \left(\frac{P_{TEG}/\eta_G}{\omega_{nom}}\right)\omega_{EF} & (\omega_E/\omega_{nom}) \ge 0.84 \end{cases} \quad (17)$$

where P_E is electrical power produced by the expander, P_{TEM} and P_{TEG} (see Table I) are expander motor torque control power supply (at nominal speed) to accelerate the rotor and the expander generator torque control power product (at nominal speed), respectively, and η_G is the equivalent generator efficiency. Note that with these definitions, the consumed power (during expander acceleration) is $(\tau_G\omega_E)/\eta_M$, while normal produced power is $\eta_G(\tau_G\omega_E)$. When an expander is placed in "run" state by the hybrid farm supervisory controller, it is first accelerated from its current speed, to the threshold speed given by $N = 0.84$ ($\omega_{Et} = 0.84\omega_{nom}$), with $m_{Ao} = 0$. At the threshold speed, compressed air discharge is started and is regulated according to the operating path on the expander map as stated above, while the power production is controlled as in (17). Presently, P_{TEG} is fixed at the value that optimized

expander power generation over the allowed expander rotor speed range. Fig. 3 (b) shows a simulation of the expander transient response from near zero initial speed. For an expander in "not run" state, $\tau_G \omega_E = 0$, there is no air flow $m_{Ao} = 0$, and the expander coasts down. If the associated air storage tank of an expander becomes empty ($p_T \leq 52$ atm), the expander is commanded into "not run" state.

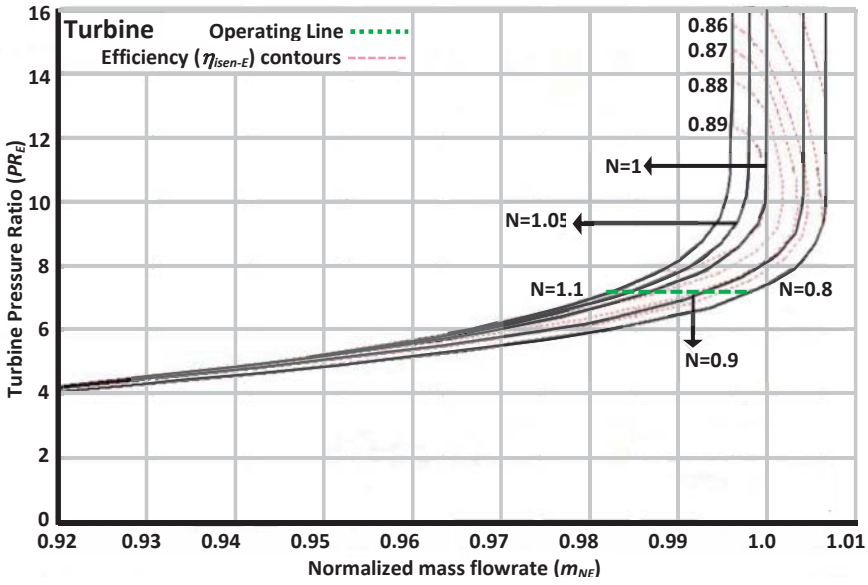

Fig. 4 Adopted expander map and operating line

D. Heat Network

The compressor ICR and ACR and the expander PHR and RHR are represented by tube-in-shell heat exchangers with the cooled or heated air flowing in the shell and the heated or cooled fluid (water), from the cold water network (CWN) or the hot water network (HWN), respectively, flowing through the tubes. While the CWN and HWN were envisaged in [13] as complete fluid circuits with complement of pumps, valves, controls and makeup systems, here they are simply modeled as constant temperature and pressure sources or reservoirs of cold water (temperature $T_{CWN} = T_a$, pressure $p_{CWN} = p_a$) and hot water (temperature T_{HWN}, pressure p_{HWN} > water saturation pressure at T_{HWN}). A single heat exchanger design (internal diameter of tubes D_{it}, number of tubes n_t, and overall length of tubes L_t) was used for the ICR, ACR, PHR, and RHR, so that, with the inlet and outlet temperatures fixed for both the air and water streams, only the requisite cold or hot water mass flowrates and hence required pump powers are sought.

The compressible-flow energy equation for a single-stream device may be expressed [20], by a thermal energy balance equation (18) and a mechanical energy balance equation (19):

$$(u_e - u_i)_{water} - \frac{\dot{Q}_{air-water}}{m_{water}} = e_{mech,loss} \tag{18}$$

$$w_{shaft,in} + \frac{P_i}{\rho_i} + \frac{{v_i}^2}{2} + g z_i = \frac{P_e}{\rho_e} + \frac{{v_e}^2}{2} + g z_e + e_{mech,loss} \tag{19}$$

where subscripts i and e connote inlet and exit conditions respectively, and $e_{mech,loss}$ represents process irreversibilities such as friction. For a practical design of the heat exchangers, (18) and (19), with $e_{mech,loss}$ given by pipe friction and entrance and exit losses (note that these are implicit functions of m_{water}), yield pumping power $m_{water}(w_{shaft,in})$ values that are not significant compared to the compressor power inputs, for nominal compressor operation and modest lengths of pipe between the reservoirs and heat exchangers. Hence in the absence of detailed and specific configurations of the CWN and HWN, power consumption in the heat networks is ignored in the performance simulations here.

E. Wind Turbine System

Under the scope of this investigation, all the wind turbines on the wind farm are represented by the same simplified NREL 5 MW baseline turbine model. With the focus primarily on integration of distributed CAES in the wind farm, load mitigation, power curtailment and reference power tracking, and power output optimization considering wake effects, are all presently omitted from the control objectives of the local wind turbine.

State Model: While the dynamics of wind turbines are well described by available advanced simulators such as FAST [21], their complexity will limit their application to the unified simulation of a hybrid wind farm, as undertaken here. We adopt instead a much reduced state space representation of the wind turbine, in particular, the six-state (it assumes constant wind direction and hence excludes a state for the yaw angle) representation of the 5MW offshore three-bladed upwind turbine with collective pitch control, employed in [22],

$$\frac{d\omega_r}{dt} = \frac{1}{I_r}\left[\frac{\rho \pi {r_r}^2 C_P(\lambda,\beta)}{2\omega_r} {v_w}^3 - K_d \gamma - B_d\left(\omega_r - \frac{\omega_g}{N_g}\right)\right] \tag{20}$$

$$\frac{d\omega_g}{dt} = \frac{1}{I_g}\left[-\tau_g + \frac{\eta_d}{N_g}\left\{K_d\gamma + B_d\left(\omega_r - \frac{\omega_g}{N_g}\right)\right\}\right] \quad (21)$$

$$\frac{d\gamma}{dt} = \omega_r - \frac{\omega_g}{N_g} \quad (22)$$

$$\frac{d\tau_g}{dt} = -\frac{1}{\Gamma_g}\tau_g + \frac{1}{\Gamma_g}\tau_{gc} \quad (23)$$

$$\frac{d\beta}{dt} = \Omega_p \quad (24)$$

$$\frac{d\Omega_p}{dt} = -{\omega_0}^2\beta - 2\xi_p\omega_0\Omega_p + {\omega_0}^2\beta_c \quad (25)$$

where ω_r = angular wind turbine rotor speed; ω_g = angular wind turbine generator speed; γ = wind turbine drive train torsion angle; τ_g = wind turbine generator torque; β = collective pitch angle; and Ω_p = time rate of change of collective pitch angle, are the six state variables, v_w = wind speed faced at the wind turbine, is a disturbance input; and τ_{gc} = wind turbine generator torque control; and β_c = collective pitch angle control, are the control inputs. The wind turbine model parameters are defined in Table II, along with their simulation values. The turbine power coefficient function $C_P(\lambda,\beta)$, where $\lambda = r_r\omega_r/v_w$ is the tip speed ratio, is assumed stationary with respect to wind speed and similar to the approach in [23], available power coefficient simulation data for the 5MW NREL wind turbine, is approximated here by the following generalized polynomial:

$$C_P(\lambda,\beta) = 10^{-6}\begin{bmatrix} -644237.787033 + 376955.566084\lambda + 33059.769597\beta - 42067.223429\lambda^2 \\ -1260.293664\lambda\beta - 3320.688883\beta^2 + 1783.918195\lambda^3 - 2582.691180\lambda^2\beta \\ +1768.169132\lambda\beta^2 + 748.246434\beta^3 - 26.568159\lambda^4 + 395.339474\lambda^3\beta \\ -440.618349\lambda^2\beta^2 - 371.062573\lambda\beta^3 - 37.892151\beta^4 - 14.342362\lambda^4\beta \\ +30.321396\lambda^3\beta^2 + 58.534216\lambda^2\beta^3 + 12.679485\lambda\beta^4 - 0.762173\lambda^4\beta^2 \\ -3.282052\lambda^3\beta^3 - 0.765576\lambda^2\beta^4 \end{bmatrix} \quad (26)$$

TABLE II
SIMULATED WIND TURBINE MODEL AND CONTROLLER PARAMETERS

B_d = 6.215x10^6 kg.m^2.rad^{-1}.s^{-1}	Drive train torsional damping constant
I_g = 534.116 kg m^2	Wind turbine generator inertia
I_r = 38.76x10^6 kg m^2	Wind turbine rotor inertia
K_d = 867.637x10^6 kg.m^2	Drive train torsional stiffness constant
N_g = 97	Wind turbine gear box ratio
$P_{W,RM}$ = 5.29661 x10^6 W	Wind turbine rated mechanical power
r_r = 63 m	Wind turbine rotor radius
η_d = 0.97	Drive train efficiency
η_g = 0.944	Wind turbine electrical generator efficiency
ρ = 1.225 kg.m^{-3}	Air density
Γ_g = 0.02 s	Generator drive 1st order closed-loop transfer function time constant
ω_0 = 11.11 Hz	Pitch drive 2nd order closed-loop transfer function natural frequency
$\omega_{g,nom}$ = 122.8990 rad/s	Wind turbine rated generator speed
ξ_p = 0.6	Pitch drive 2nd order closed-loop transfer function damping ratio
$C_{\tau,2}$ = 2.2438 N.m. rad^{-2}.s^{-2}	Region 2 torque constant
$f_{g,c}$ = 0.25 Hz	Generator speed low-pass filter corner frequency
Γ_{WC} = 0.025 s	Wind turbine controller time step
β_{max} = 90 deg	Maximum pitch angle setting
β_{min} = 0 deg	Minimum pitch angle setting
$\beta_{m,\tau3}$ = 1 deg	Minimum pitch angle ensuring region 3 torque
β_{2s} = 6.30234 deg	Pitch angle at which pitch sensitivity doubles
β_{rate} = 8 deg/s	Maximum absolute pitch angle rate
κ_{P0} = 1.07859 deg.s/rad	Proportional gain at minimum pitch angle setting
κ_{I0} = 0.46225 deg/rad	Integral gain at minimum pitch angle setting
$\tau_{g,max}$ = 47403 N.m	Maximum wind turbine generator torque
$\tau_{g,rate}$ = 15000 N.m/s	Maximum wind turbine generator torque rate
$\omega_{g,t3}$ = 121.6700 rad/s	Transition generator speed between regions 2½ and 3
$\omega_{g,t1}$ = 70.1310 rad/s	Transition generator speed between regions 1 and 1½
$\omega_{g,t2}$ = 91.1703 rad/s	Transition generator speed between regions 1½ and 2

$\omega_{g,S3} = \omega_{g,t3}/1.1$; $S_{\tau,2} = C_{\tau,2}(\omega_{g,t2})^2/(\omega_{g,t2}-\omega_{g,t1})$; $P_{S3} = C_{\tau,2}(\omega_{g,S3})^2$; $S_{\tau,3} = (P_{W,RM}/\omega_{g,t3})-P_{S3}/(\omega_{g,t3}-\omega_{g,S3})$

The peak power coefficient $C_{P,max}$ = 0.4853 occurs at (λ^* = 7.6, β^* = 0°).

Wind Turbine Control: For the local wind turbine control, we implement, considering the stated focus of the simulations, the simple algorithm of the legacy controller for the 5-MW wind turbine [21], that maximizes power generation by controlling

torque below a rated wind speed, and by regulating the turbine power at the rated level with collective blade pitch control based on a gain-scheduled proportional-integral (PI) control system, above the rated wind speed. Fig. 5 summarizes this control algorithm, for a generic wind turbine-*n*. The controller parameters are also defined in Table II with their simulation values. Note that generation of the low-pass filtered output $P_{WF,n}$ shown in dashed outline in Fig. 5, is strictly not a part of the wind turbine controller, but part of the feed forward of the hybrid farm CAES-wind turbine station signals to the farm supervisory controller. The filter dynamics is given by,

$$\frac{dP_{WF}}{dt} = \frac{1}{\Gamma_v}\left(\omega_g \tau_g - P_{WF}\right) \tag{27}$$

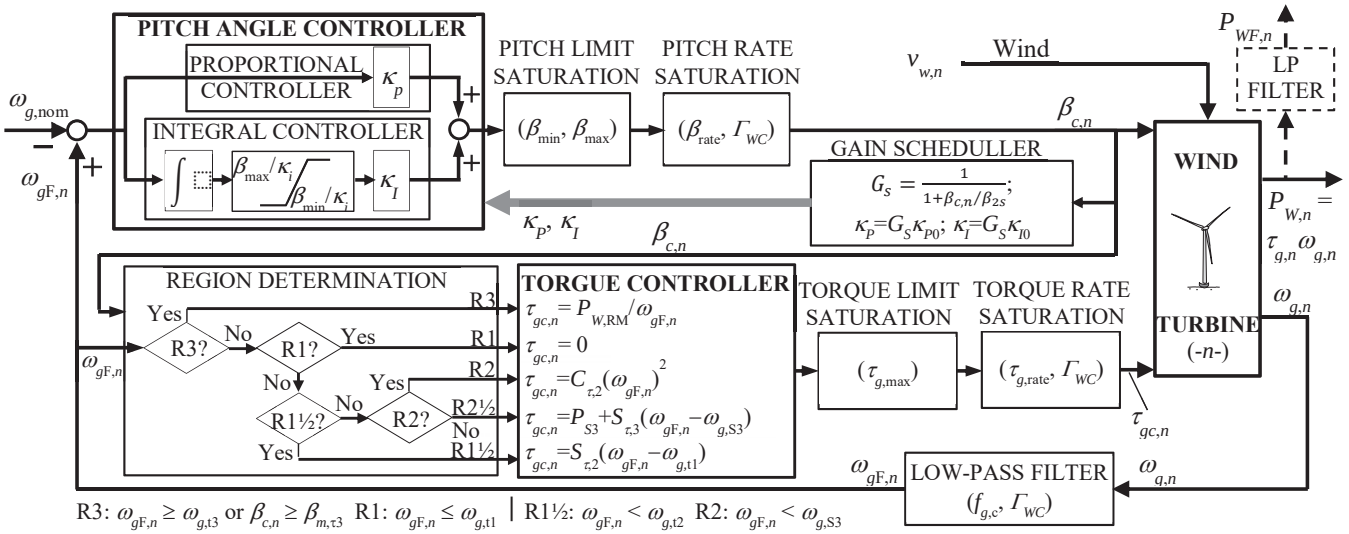

Fig. 5 Region based wind turbine controller

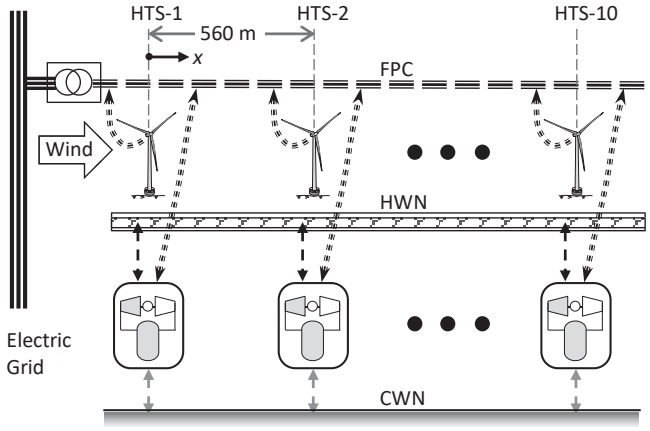

Fig. 6 Hybrid wind farm layout

where the time constant $\Gamma_v = 10$s is chosen considering that the input wind speed dynamics is much faster than the dynamics of the wind turbine generator speed. In the simulation, (27) was represented by a discrete-time expression based on the wind turbine controller time step, hence the placement of this filter circuit in the wind turbine controller block. As a practical matter, $P_{WF,n}$ could be estimated from a low-pass filtered wind speed measurement or a forecast of the instantaneous wind speed at wind turbine-*n*, instead of the low-pass filtered measurement of the wind turbine-*n* generator power.

F. Hybrid Wind Farm System

The hybrid wind farm consists of a number of wind turbines with CAES stations distributed over a geographic area. Each wind turbine is located on the farm by its longitudinal coordinate *x*, assumed parallel to the prevailing wind direction, and lateral coordinate *y*, which is perpendicular to the longitudinal coordinate. For a computationally manageable yet adequate representation, however, only a wind farm containing ten such wind turbine stations on a single (longitudinal) row, as illustrated in Fig. 6, is simulated. The simulated hybrid wind farm also includes 10 CAES stations, one for each wind turbine, as shown in the figure. Aerodynamic interaction between the wind turbines is included in the simulations by a simplified wind field wake model which determines the local wind speed $v_{w,n}$, faced by each wind turbine-*n*.

Wind Field and Wake Model: The objective for the wind field model is a plausible wind distribution with realistic wake effects and manageable computational load. The Jensen wake model employed in [22] was adopted, except that the wind field was not static but subject to these simplifying assumptions:

1. The process uses actual wind data that may be treated as deterministic and available at a measurement point, which is the origin of coordinates at the front of the farm, as a discrete-time series or sampled data $v(\kappa\Gamma_w)$, with mean values $v_m(\kappa\Gamma_w)$, $\kappa = 0, 1, 2, \ldots$; Γ_w = sampling period.
2. The wind speed time series within fixed time intervals (the mean wind speeds are constant over these time intervals, that is $v_m(\kappa\Gamma_w)$ is a staircase pattern), travels down the field at the relevant mean wind speed: thus, at time $t = \kappa_t\Gamma_w$, at a given wind turbine *j*, located a distance *d* downstream of the measurement point, the ambient wind speed (the wind speed if no other turbines were present) is

$$v_j(t) = v(t_\kappa) \ni d/v_m(t_\kappa) \le (t - t_\kappa),\ t_\kappa = \kappa_t \Gamma_w,\ (\kappa_t - 1)\Gamma_w,\ (\kappa_t - 2)\Gamma_w, \ldots \quad (28)$$

3. The time interval is adequately chosen considering both the longitudinal extent of the farm, the overall mean speed of the wind record, and the detailed shape/pattern of the wind speed record.

The wake model gives the fractional wind velocity deficit caused at downstream coordinates (x,y), by a wind turbine j located at (x_j,y_j) as,

$$\delta v_j(\Delta x_j, \Delta y_j, C_{Tj}) = \begin{cases} \frac{1}{2} C_{Tj} \left(1 + \frac{\Delta x_j}{4r}\right)^{-1} & \text{if } \Delta y_j \le \sqrt{4{r_r}^2 + r_r \Delta x_j} \\ 0 & \text{if } \Delta y_j > \sqrt{4{r_r}^2 + r_r \Delta x_j} \end{cases} \quad (29)$$

where $\Delta x_j = (x - x_j)$, $\Delta y_j = (y - y_j)$, and $C_{Tj} = C_{Tj}(\lambda_j,\beta_j)$ is the turbine thrust coefficient. As it was the case with the turbine power coefficient, available thrust coefficient data $C_T(\lambda,\beta)$ for the 5MW NREL wind turbine, are approximated here by the following generalized polynomial:

$$C_T(\lambda,\beta) = 10^{-6} \begin{bmatrix} -96514.2603231 + 157071.771795\lambda - 9459.026633\beta - 7604.765227\lambda^2 \\ +6705.628283\lambda\beta + 979.9483327\beta^2 + 204.052079\lambda^3 - 1506.067006\lambda^2\beta \\ -664.341934\lambda\beta^2 + 404.549342\beta^3 - 1.542475\lambda^4 + 23.639000\lambda^3\beta \\ +15.627606\lambda^2\beta^2 - 160.377976\lambda\beta^3 - 22.666110\beta^4 - 0.492621\lambda^4\beta \\ +2.122416\lambda^3\beta^2 + 7.079183\lambda^2\beta^3 + 7.9985897\lambda\beta^4 \end{bmatrix} \quad (30)$$

Since the wind turbine tip speed ratio λ_j is a function of the wind speed, C_{Tj} is a function of the "actual" wind speed at turbine j, $v_{w,j}(t)$. Note that (28) gives $v_j(t)$, the wind speed at turbine j in the absence of any upwind turbines, and not the "wake-affected" wind speed at turbine j, $v_{w,j}(t)$. The wake-affected wind speed at any wind turbine n, located at coordinates (x_n,y_n), is a function of the aggregate wind velocity deficit due to all the wind turbines upwind of turbine n:

$$v_{w,n}(t) = v_n(t) \left[1 - \sqrt{\sum_{j \in \mathbf{W}_n} \left\{ \delta v_j(\Delta x_j, \Delta y_j, C_{Tj}) \frac{\hat{A}_{j \to n}}{A} \right\}^2}\right] \quad (31)$$

where W_n is the set of wind turbines upwind of wind turbine n, $A = \pi {r_r}^2$ is the swept area of the wind turbine-n rotor and $\hat{A}_{j \to n}$ is the area of the overlap between area A at (x_n,y_n), and the area at (x_n,y_j) swept by the radius ($r = \sqrt{4{r_r}^2 + r_r(x_n - x_j)}$) of the wake generated by turbine j. To facilitate simulation of (31), the thrust coefficients computed at each time $t = \kappa_t \Gamma_w$, are stored sequentially in a buffer for each wind turbine on the farm.

Hybrid Farm Controller: As previously explained, the wind farm control approach explored here focuses on the CAES system as the primary means of tracking TSO power demand for the farm while leaving the individual wind turbines to merely produce as much power as possible from the available local wind. This is only a simplified focus and does not preclude situations where TSO power tracking is shared between the wind turbines and the CAES system; and the control of the wind turbines also includes other objectives such as load mitigation. With the hybrid wind farm active power control (APC) limited to the CAES system, the transient behavior of the compressors and expanders are significant considerations. As is evident in Fig. 3, both the compressor and the expander, on command to produce compressed air or generate power, respectively, undergo periods of varying length depending on starting speed, during which the compressed air is not produced or the power is not generated. For the expander, power is even consumed during this interval. Further, the power consumed by the compressor or produced by the expander, following this initial period, is not instantaneously fixed but ramps to a steady value in finite time. In lieu of a complex (compressor and expander) model-referenced supervisory controller, an ad hoc static prescriptive hybrid farm controller algorithm is first investigated here.

Fig. 7 summarizes the control algorithm. The supervisory controller inputs are: the reference power demand signal from the TSO, P_D; the individual wind turbine station low-pass filtered electrical power production $P_{WF,n}$; and the individual CAES control loop outputs, including the expander rotor speed and power production $\omega_{E,n}$ and $P_{E,n}$, the compressor rotor speed and power consumption $\omega_{C,n}$ and $P_{C,n}$, the state of charge of the air storage tanks $M_{T,n}$, and (although not directly indicated in the figure) the run states of the expanders and the compressors [off (not necessarily stopped but could be coasting), on but not producing, and on and producing]. The output, or set points to the local CAES stations, include: running expanders and compressors shut, not running expanders and compressors started, and the power consumption level setting for running compressors. Note that the local compressor controller applies the power consumption level setting if or when the compressor is at or above the threshold speed ω_{Ct}.

Following the outline in Fig. 7, a CAES state preprocessor uses the input information to first shut expanders whose air storage tank is near "empty", that is the tank would otherwise reach empty by the end of the supervisory controller cycle time, and shut compressors whose storage tank is near "full", that is the tank would otherwise be full by the end of the supervisory controller cycle time under nominal operations; generate for each CAES station-n, an eight-states status "vector" $SC_{n,s}$ and the "aggregate" CAES status $SC_{T,s}$, s = 1, 2, ..,8, which are described in Table III; and compute the current total CAES power production CAP. Note that the supervisory controller cycle time (60 seconds, in this case) is orders of magnitude larger than the local wind turbine and CAES station controls time step (Γ_{WC} = 0.025 s) and the critical action of shutting expanders and compressors is assigned to the supervisory

controller in the present implementation and not to the local CAES control loop. The individual wind turbine filtered power production input $P_{WF,n}$, is summed to yield the total power production of wind turbines in the wind farm *TWP*, and the differential hybrid wind farm power production $DFP = CAP + TWP - P_D$ is computed, as indicated in the figure.

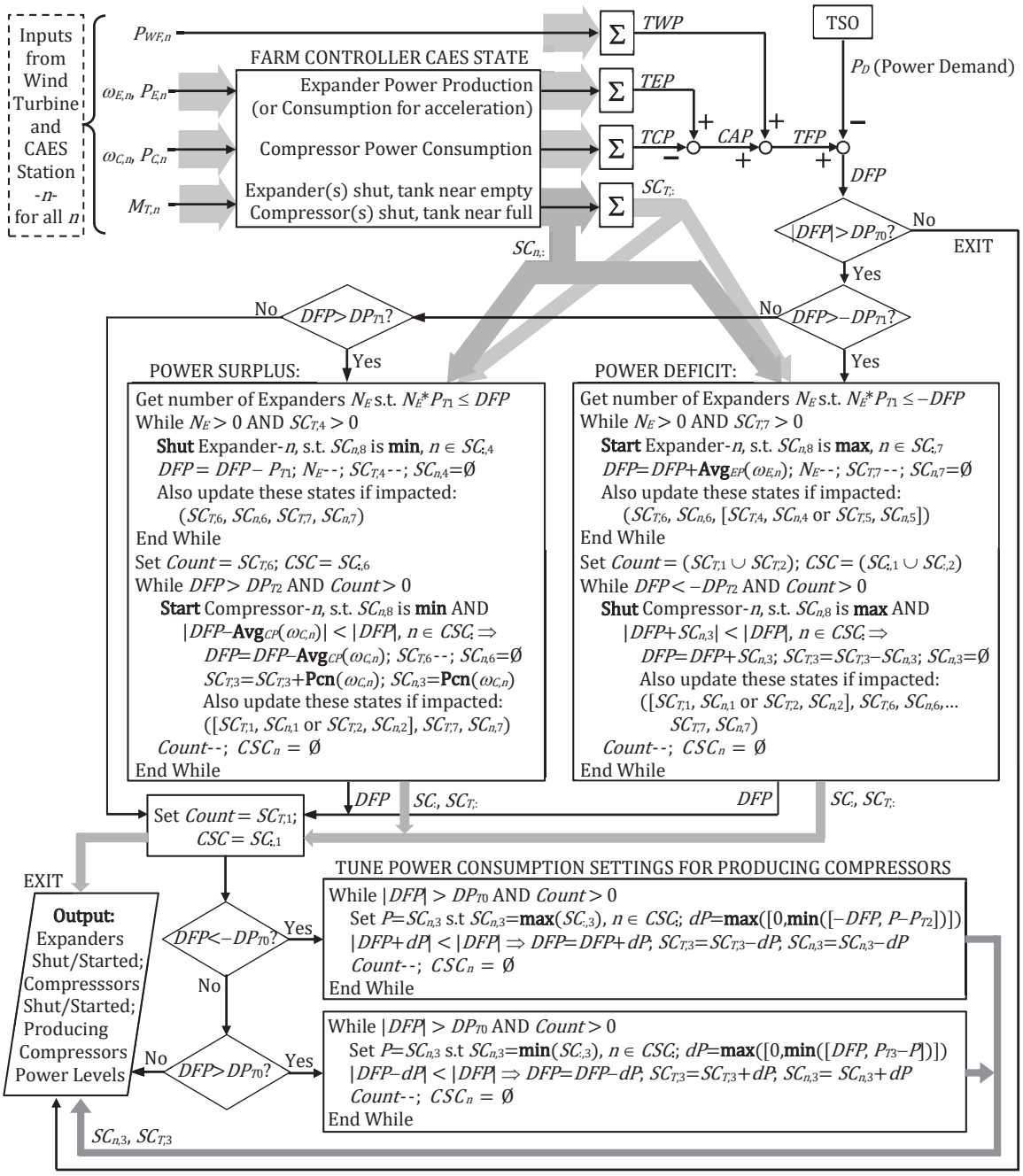

Fig. 7 Flowchart of hybrid farm supervisory controller

No further action is taken by the supervisory controller, if the absolute value of this *DFP* is not more than a threshold power (error) value DP_{T0} (equal to 0.25 MW in the simulations). Otherwise, a *Power Deficit* controller decision path is followed if $DFP < -DP_{T1}$, where $DP_{T1} = ½ P_{T1}$ and P_{T1} (here 4.0621 MW) is the expander steady state electrical power production determined from simulation, as in Fig. 3 (b), when the generator control torque is given by P_{TEG} (see Table I); or a *Power Surplus* path is followed if $DFP > DP_{T1}$. Fig. 7 outlines the algorithmic decisions taken along each of the two paths. For the *Power Deficit* path, a feasible number of expanders are started as well as some running compressors (producing or not) may be shut, as necessary, if the balance deficit, after starting expanders is more than DP_{T2}, and there are available running compressors to

shut. $DP_{T2} = ½ P_{T2}$ and P_{T2} (here 3.2623 MW) is the compressor steady state electrical power consumption determined from simulation, as in Fig. 3 (a), when the motor control torque is given by $P_{TC,\min}$ (see Table I). To ameliorate the deleterious effect of the complex transient response of the expander, the deficit reduction for a started expander is taken as the average of the immediate expander power production (which could be negative depending on the rotor speed) and the projected power production at the end of the supervisory controller cycle. This average power is approximated by the function $\mathrm{Avg}_{EP}(\omega_E)$, which presently uses a bilinear approximation of the expander transient response of Fig. 3 (b) (a negative ramp of constant slope prior to threshold rotor speed ω_{Et}, followed by fixed power production of value P_{T1} beyond threshold speed).

TABLE III
CAES STATION STATES AND AGGREGATE STATUS FOR ALL STATIONS

State	Description of CAES state $SC_{n,:}$	Aggregate status $SC_{T,:}$
1	Compressor is running and producing compressed air	Number of such compressors
2	Compressor is running but not producing (merely accelerating)	Number of such compressors
3	Power being consumed by running compressor	Total power for compressors
4	Expander is running and producing power	Number of such expanders
5	Expander is running but consuming power (merely accelerating)	Number of such expanders
6	Compressor and expander not running but compressor may start	Number of such stations
7	Compressor and expander not running but expander may start	Number of such stations
8	State of charge of (amount of compressed air in) storage tank	Total amount of stored air

In a similar manner, the *Power Surplus* path shuts a feasible number of expanders, and starts compressors, as necessary, if the balance surplus, after shutting expanders is more than DP_{T2} and there are available compressors to start. The contribution to the surplus reduction of started compressors is taken as the average of the immediate compressor power consumption (this value which is also utilized in the algorithm is represented by the function $\mathrm{Pcn}(\omega_C)$) and the projected power consumption at the end of the supervisory controller cycle. This average power consumption is approximated by the function $\mathrm{Avg}_{CP}(\omega_E)$, which also uses a bilinear approximation of the compressor transient response of Fig. 3 (a). However, since a running and producing compressor's steady power consumption is also determined by the supervisory controller, the $\mathrm{Avg}_{CP}(\omega_E)$ function uses the minimum power consumption level P_{T2}, as a base or starting value for the desired compressor steady state power consumption level. Tuning of the producing compressors' power consumption settings is carried out, as outlined in Fig. 7, to further reduce the error between the hybrid farm power production and the TSO power demand when the eventual $|DFP|$ is still more than DP_{T0}. The quantity P_{T3} (here 4.9085 MW) referenced in the last block in Fig. 7 is the compressor steady state electrical power consumption determined from simulation, as in Fig. 3*a*, when the motor control torque is given by $P_{TC,\max}$ (see Table I).

III. SIMULATION RESULTS

The external input data used in the simulations and the simulation results obtained by MATLAB using a fixed-step fourth-stage Runge-Kutta method, are discussed in the following. These results reflect the configuration choices and design assumptions described in the forgoing and may not be generalized arbitrarily.

A. Wake Effect and Wind Speed Record

Fig. 8 shows the wind speed data used in the simulations (a) and the wind turbine electrical power generation at a number of wind turbine stations on the wind farm (station 1 – (b), station 4 – (c) and station 10 – (d)). The power generation at wind turbines geographically distributed on the wind farm displays the anticipated trends, including the wake effects of changes in wind speed and turbulent content. The wind speed data were derived from actual wind record (logged data by Horns Rev SCADA on 01/18/2001, at 40 m height; see broader data base description in [24]), which consisted of eight hours of wind speeds (in m/s) measurement at a sampling period of $\Gamma_w = 0.05$ s, and mean wind speeds averaged at 10-minute intervals throughout. These data were then adjusted to the 90 m hub height assumed for the NREL 5 MW wind turbine model, using the following power law [25] expression:

$$v_{w,1} = v_r \left(\frac{H_h}{H_r}\right)^{\alpha};\ \alpha = \frac{0.37 - 0.088 \ln(v_r)}{1 - 0.088 \ln\left({}^{H_r}/_{10}\right)} \tag{32}$$

where v_r is the reference wind speed data value (in m/s), H_r (40 m) is the reference height, H_h (90 m) is the hub height and $v_{w,1}$ is the wind speed value at hub height (in m/s), which in this case, is also the wind speed faced at the first wind turbine station on farm. The instantaneous wind speeds faced at downstream wind turbine stations were determined according to the wake model described in Section II *F*. In this regard, it should be noted that the first 600 seconds of the adjusted wind speed data were repeated at the front of the record to serve as a disposable startup phase in which only the wind turbines are run (neither the CAES system nor the hybrid farm supervisory controller are active and no results are recorded) to permit orderly system initialization and, in particular, seeding of the historic buffer of wind turbine thrust coefficients, required by the transient wake field model.

B. TSO Power Signal and Hybrid Farm Controller Performance

Fig. 9 shows the 8-hour TSO power demand signal used to simulate the hybrid wind farm power response subject to the ad hoc CAES hybrid wind farm supervisory controller. The data are derived from the total wind farm power setpoint in a reported dynamic performance data for Horns Rev offshore wind farm for, as described in [26], a "normal" day operation in which several of the control functions in the wind farm main controller (WFMC) were active simultaneously. The graphic data were sampled at 3-minute intervals and scaled such that the maximum setpoint value is 50 MW which is the total power rating for the present 10-wind turbine simulated wind farm.

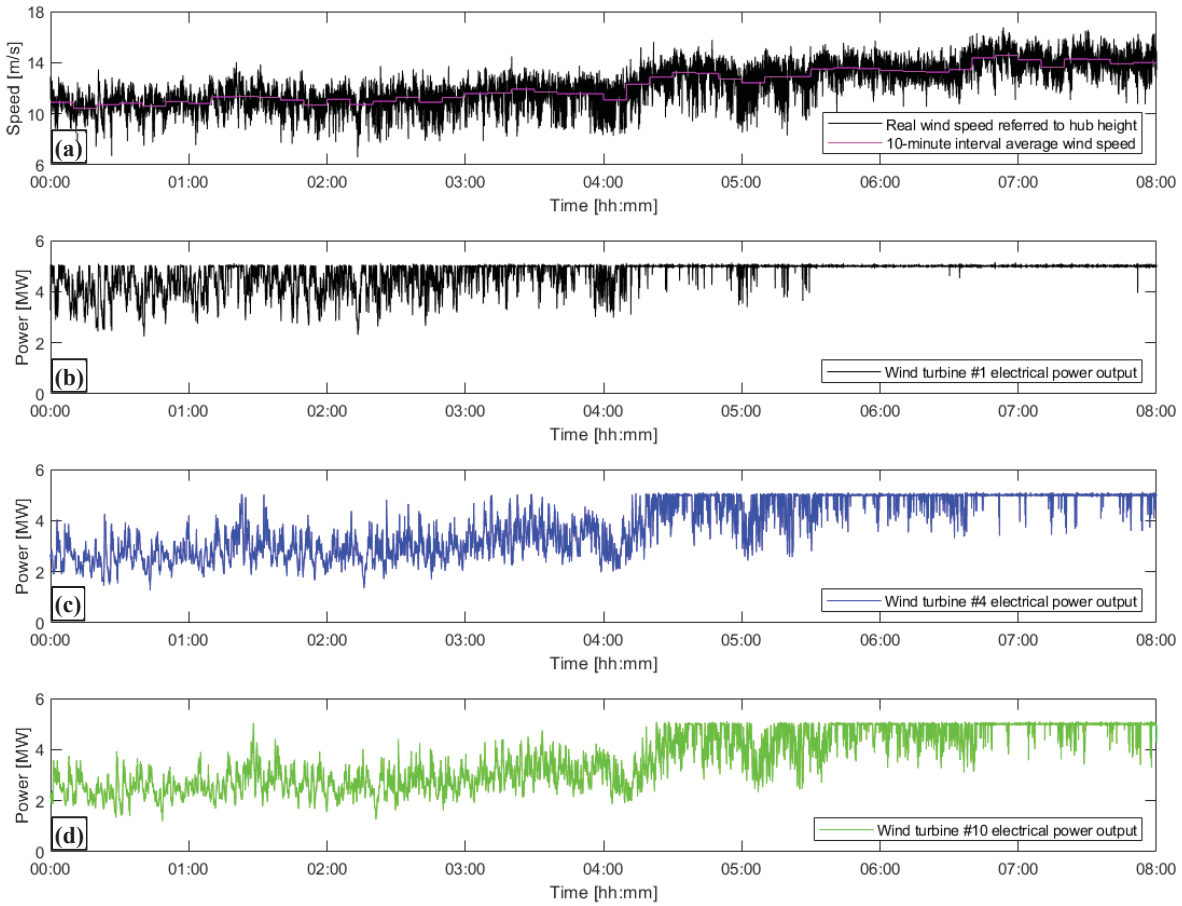

Fig. 8 Simulation wind data and power response of wind turbines in the wind farm

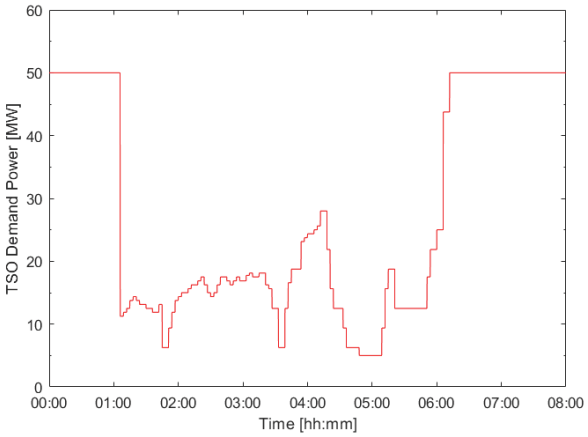

Fig. 9 TSO power demand signal

Fig. 10 shows the TSO power reference signal and the total power production of the hybrid wind farm (wind turbines and CAES stations) under the ad hoc supervisory hybrid farm control. While a 3-minute scale power demand signal is assumed, a 1-minute (60 s) supervisory controller cycle time was adopted as reasonably fast and feasible for an average size hybrid wind farm. It can be observed that the instantaneous total hybrid wind farm output (combined net CAES and unfiltered total wind power) tracks the TSO power demand signal quite well, with deviations, generally within an error band of about the size of a single expander power production. However, some somewhat larger power output excursions are observed in the response due to the partial capacity of the present hybrid farm control algorithm to adequately compensate for the CAES power switching disruptions within the hybrid controller cycle period following controller commanded stop or start of an expander and or compressor, including when an associated air storage tank becomes “empty” or full. The power excursions may be observed in the record of the net power output from all CAES stations which is also shown in Fig. 10.

The ten CAS tanks were initialized in all the simulations with a somewhat arbitrary state of charge pattern represented by the vector [1, 0.9, 0.8, 0.7, 0.6, 0.5, 0.5, 0, 0, 0], with “1” representing a full tank (first station storage tank in this case) and “0” representing an empty tank (storage tanks of the last three stations, in this case). Note that an empty tank implies that the tank pressure is down to 52 atm, not zero stored air mass. Fig. 10 also displays the total power output of the wind turbines, which is not affected by the supervisory controller action due to its implementation in the present investigation.

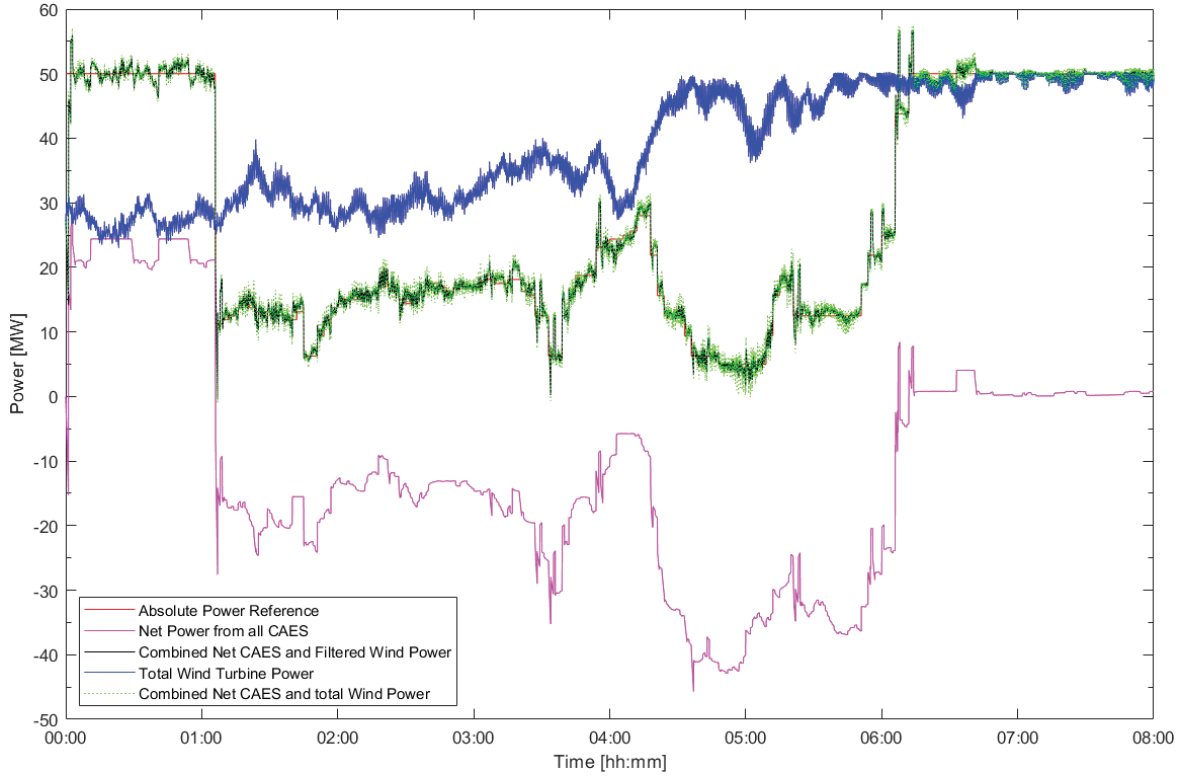

Fig. 10 Power reference tracking of hybrid wind farm output under ad hoc controller

C. Distributed CAES in Hybrid Wind Farm Efficiency

A number of single-parameter performance indices proposed for conventional D-CAES were discussed by [1]. A typical performance index based on the electrical energy generated by the expander E_E, the electrical energy delivered to the compressor motor E_C, and the energy in the fuel E_F, is:

$$\eta_{cycle} = \frac{E_E}{E_C + \eta_{fte} E_F} \tag{33}$$

where $\eta_{fte}E_F$ is the amount of electricity that could have been made from the fuel (heat) input E_F. η_{fte} depends on the basic power plant process emulated for the computation but reported values in the literature are generally below 0.5. In applications of (33) type efficiency definitions in the literature, such as in [27] and [28], one or more conventional CAES charge-discharge cycles is employed. Moreover, for each cycle, it is the compressed air accumulated during the charge phase that is used up in the discharge phase. This scenario is quite different from the situation with a distributed CAES system, for which multiple compressors and expanders could be charging and discharging simultaneously. Moreover, the necessity for coordination of such simultaneous charging and discharging processes implies that the influence on system efficiency of the particular distributed CAES system controller, and even the process by which the energy is delivered to the CAES system, could be significant considerations. While (33) is employed to compute a distributed CAES round trip efficiency for comparison purposes, a comprehensive and perhaps more representative but simulation-based overall distributed CAES in hybrid wind farm efficiency is suggested as follows:

$$\eta_{Dsys} = \frac{P_{DB}\Delta t_S}{\int^{\Delta t_S}(\Sigma_n P_{W,n})dt + \eta_{fte}\int^{\Delta t_S}(m_F LHV)dt} \tag{34}$$

where Δt_S is a simulation time interval of sufficient length, P_{DB} is a fixed reference power tracked by the distributed CAES system, such that the total state of charge of the storage tanks in the system is the same at the end of the simulation as it was at the beginning, and $(\Sigma_n P_{W,n})$ is the total instantaneous power delivery to the CAES system, which is, in this case, the total power produced by the wind turbines.

Fig. 11 shows the result of the suggested simulation for the present investigation, using the 8-hour simulation time and the same input wind speed data described previously. The value of P_{DB} obtained by trial-and-error with a resolution of 10 kW, is 34.04 MW (the starting and ending total compressed air mass was 1707600 kg and 1701000 kg or 99.6% of start value, respectively), the total electrical energy input from the wind turbines is 1.1774×10^{12} J, and the total fuel heat input is 3.8097×10^{10} J. Using a value of 0.5 for η_{fte}, (34) yields the overall efficiency η_{Dsys} = 81.94%. Note that only a very marginal increase in the efficiency would be obtained if P_{DB} in (34) is replaced by the combined net CAES and wind turbine power (dotted green trace in Fig. 11).

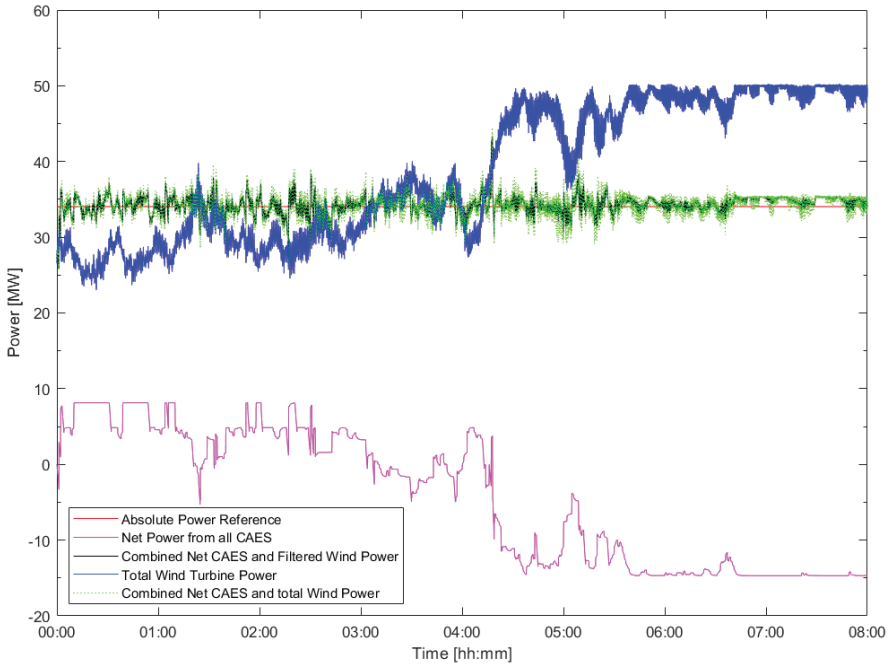

Fig. 11 Hybrid wind farm response to fixed setpoint

Now, using the same data obtained from the simulation of Fig. 11, the distributed CAES round trip efficiency may be computed for comparison to reported values in the literature. The net total expanders electrical energy output is 1.2259×10^{11} J, while the total electrical energy consumed by the compressors is 2.4655×10^{11} J. Using the already stated value for total fuel heat input, (33) gives $\eta_{cycle} = 46.16\%$, which is comparable with reported values in the literature for D-CAES systems, including configurations with efficiency enhancing compression stage ICR s and ACR and LpE recuperator. For example, [27] reports primary energy efficiency of 47% and [28] reports global efficiencies that varied from 43.64% for a wind farm with 140 wind turbines, to 46.29% for a 20 wind turbines wind farm. Some reported that round trip efficiencies for A-CAES are also not significantly higher. Round trip efficiency values computed by [7] varied from 63.9% in the first cycle to an average of 64.7% in subsequent cycles, for a dynamic A-CAES model using pressurized hot water tank for thermal energy storage, while the packed bed thermal energy storage based A-CAES in [8] reported round trip efficiencies that varied from about 53% in the first cycle to an average of 64% in subsequent cycles, under a partial-load causing charge-discharge cycle power profile. However, in addition to the absence of effects of CAES controller action and input power dynamics, in these examples, it is noted that the cycle simulations of [7] apparently do not induce part load operation of the turbomachinery, while the turbomachine models in [8] do not include rotor inertia and friction.

IV. Conclusion

A dynamic model of a hybrid wind farm with distributed D-CAES, using air storage tanks and compressor and expander trains at each wind turbine station is developed and simulated using MATLAB with real wind data and TSO absolute power reference signals as inputs. The simulation results show that a proposed ad hoc supervisory controller for scheduling and regulating compressed air production and only CAES power generation is able to track the minute-scale power demand signal within an error band size comparable to the electrical power rating of a single expander. While conventional wind farm power control systems require significant curtailment of individual wind turbine power production due to the uncontrollability of natural wind input, the present hybrid wind farm with distributed CAES control result suggests that combining a global distributed D-CAES controller with power regulation for individual wind turbines could further improve the system's performance, as well as, minimize the amount of wind turbine power curtailment necessary in such a wind farm control scheme. These findings contribute to the existing knowledge of integrating CAES with wind farms that are without access to large-scale storage or underground caverns, thereby enhancing the thermal efficiency and capacity of such systems.

References

[1] S. Succar, and R.H. Williams, "Compressed air energy storage: Theory, resources, and applications for wind power," *Princeton Environmental Institute Report*, April 8, 2008.

[2] J. Eyer, and G. Corey, "Energy storage for the electricity grid: benefits and market potential assessment guide," *Sandia National Laboratories Report*, SAND2010-0815, Albuquerque, New Mexico. 2010.

[3] P. Denholm, E. Ela, and M. Milligan, "Role of energy storage with renewable electricity generation," *National Renewable Energy Laboratory*, NREL/TP-6A2-47187, 2010.

[4] M. Budt, D. Wolf, R. Span, and J. Yan, "A review on compressed air energy storage: basic principles, past milestones and recent developments," *Applied Energy*, vol. 170, pp. 250-268, 2016.

[5] U.S. Department of Energy, and U.S. Department of the Interior, "A national offshore wind strategy: creating an offshore wind energy industry

in the United States," February 7, 2011.
[6] E. Barbour, D. Mignard, Y. Ding, and Y. Li, "Adiabatic compressed air energy storage with packed bed thermal energy storage," *Applied Energy*, vol 155, pp. 804-815, 2015.
[7] Y. Mazloum, H. Sayah, and M. Nemer, "Static and dynamic modeling comparison of an adiabatic compressed air energy storage system," *Journal of Energy Resources Technology*, vol. 138, No. 6, 2016.
[8] A. Sciacovelli, Y. Li, H. Chen, Y. Wu, J. Wang, S. Garvey, and Y. Ding, "Dynamic simulation of adiabatic compressed air energy storage (A-CAES) plant with integrated thermal storage – link between components performance and plant performance," *Applied Energy*, vol. 185, Part 1, pp. 16-28, 2017.
[9] P.Y. Li, J.D. Van de Ven, and C. Sancken, "Open accumulator concept for compact fluid power energy storage," *Proc: Int. Mechanical Engineering Congress and Exposition* (IMECE), Seattle, WA, USA, 2007.
[10] M. Saadat and P.Y. Li, "Modeling and control of an open accumulator compressed air energy storage (CAES) system for wind turbines," *Applied Energy*, Vol. 137, pp. 603-616, 2015.
[11] X. Zhang, Y. Xu, X. Zhou, Y. Zhang, W. Li, Z. Zuo, H. Guo, Y. Huang, and H. Chen, "A near-isothermal expander for isothermal compressed air energy storage system," *Applied Energy*, vol. 225, pp. 955-964, 2018.
[12] A.V. Olympios, *et al*, "Progress and prospects of thermo-mechanical energy storage – a critical review," *Progress in Energy*, 3, 022001, 2021.
[13] E. Umez-Eronini, "Wind farm with compressed air energy storages," *European Patent* EP3259473B1, July 8, 2020.
[14] H. Sun, X. Luo, and J. Wang, "Feasibility study of a hybrid wind turbine system – integration with compressed air energy storage," *Applied Energy*, vol. 137, pp. 617-628, 2015.
[15] C Krupke, J. Wang, J Clarke, and X. Luo, "Modeling and experimental study of a wind turbine system in hybrid connection with compressed air energy storage," *IEEE Transactions on Energy Conversion*, vol. 32, No. 1, pp. 137-145, 2017
[16] H. Safaei, D.W. Keith, and R.J. Hugo, "Compressed air energy storage (CAES) with compressors distributed at heat loads to enable waste heat utilization," *Applied Energy*, vol. 103, pp. 165-179, 2013.
[17] H. Safaei, and D.W. Keith, "Compressed air energy storage with waste heat export: an Alberta case study," *Energy Conversion Management*, vol. 78, pp. 114-124, 2014.
[18] D. Li, R.A. Dougal, E. Thirunavukarasu and A. Ouroua, "Variable speed operation of turbogenerators to improve part-load efficiency," *IEEE Electric Ship Technologies Symposium* (ESTS), Arlington VA, USA, pp. 353-359, 2013.
[19] I. Urieli, *Engineering Thermodynamics – A Graphical Approach*; chapter 11 Combustion, March 2021 update, available under the Creative Commons Attribution-ShareAlike License.
[20] Y. Cengel and J. Cimbala, *Fluid Mechanics – Fundamentals and Applications*, McGraw-Hill Companies, Inc., 2006.
[21] J. Jonkman, S. Butterfield, W. Musial, and G. Scott, "Definition of a 5-MW reference wind turbine for offshore system development," *Technical Report* NREL/TP-500-38060, National Renewable Energy Laboratory, Golden CO, USA, 2009.
[22] F. Heer, P.M. Esfahani, M. Kamgarpour, and J. Lygeros, "Model based power optimization of wind farms," *European Control Conference* (ECC), pp. 1145-1150, 2014.
[23] M. Soleimanzadeh and R. Wisniewski, "Controller design for a wind farm, considering both power and load aspects," *Mechatronics*, vol. 21, No. 4, pp. 720-727, 2011.
[24] G.C. Larsen, and K.S. Hansen, "Database on wind characteristics – structure and philosophy," Risø National Laboratory, Roskilde, November 2001.
[25] C.G. Justus, and A. Mikhail, 'Height variation of wind speed and wind distribution statistics," *Geophys. Res. Letters*, vol.3, pp. 261-264, 1976.
[26] J.R. Kristoffersen, "The Horns Rev wind farm and the operational experience with the wind farm main controller," in *Proc. Copenhagen Offshore Wind 2005*, 26-28 October, pp. 1-9, 2005.
[27] Y.S.H. Najjar, and M.S. Zaamout, "Performance analysis of compressed air energy storage (CAES) plant for dry regions," *Energy Convers. Mgmt*, vol. 39, No. 15, pp. 1503-1511, 1998.
[28] I. Arsie, V. Marano, G. Rizzo and M, Moran, "Energy and economic evaluation of a hybrid power plant with wind turbines and compressed air energy storage," *ASME Power Conference*, Atlanta, GA, USA, May 2-4, 2006.